Available online at www.sciencedirect.com
SCIENCE DIRECT®
ELSEVIER
International Journal of Heat and Mass Transfer 47 (2004) 2417–2435
International Journal of HEAT and MASS TRANSFER
www.elsevier.com/locate/ijhmt

Micro-thermoelectric cooler: interfacial effects on thermal and electrical transport

Luciana W. da Silva, Massoud Kaviany *

Department of Mechanical Engineering, University of Michigan, 2250 G. G. Brown Laboratory, 2350 Hayward Avenue, Ann Arbor, MI 48109-2125, USA

Received 23 November 2002

Abstract

The flows of heat and electricity in a column-type micro-thermoelectric cooler are analyzed by modeling the various interfacial resistances. Electron (barrier tunneling) and phonon (diffuse mismatch) boundary resistances at the thermoelectric/metal interface, and thermal non-equilibrium between electrons and phonons adjacent to this interface (cooling length), increase the thermal conduction resistance and decrease the Seebeck coefficient of the thermoelectric elements. These in turn reduce the device cooling performance, which is also affected by the thermal and electrical contact resistances at the thermoelectric/metal and metal/electrical-insulator interfaces.

To produce a temperature drop of 10 K with a cooling load of 10 mW, the optimum number of thermoelement pairs, operating current, and coefficient of performance, based on vapor deposited 4 μm thick films of Bi_2Te_3 and Sb_2Te_3, are predicted for a micro-thermoelectric cooler operating with a 3 V battery.
© 2003 Elsevier Ltd. All rights reserved.

1. Introduction

Thermoelectric cooling is a suitable technique for the local cooling of micro-sensors and devices as it does not require any moving parts and can be microelectronically integrated. While the search for thermoelectric materials compatible with solid-state electronics material continues, tellurium compounds currently have the highest cooling performance around room temperature. Thin films (700 nm) of tellurium compounds have been deposited by vapor deposition [1,2]. Min and Rowe [3] proposed a micro-thermoelectric cooler where the thermoelectric thin films are grown on a very thin, low thermal conductivity SiC membrane (PECVD) to minimize the heat leakage effect. The electrical current and heat flow parallel to the film plane. Thick films (10–50 μm) of tellurium alloys have been deposited using electroplating for fabrication of thermoelectric coolers where the current and heat flow perpendicular to the film plane (column-type design) [4,5]. Yao et al. [6] have increased the performance of this design by optimizing the geometry and using suitable materials (for both the thermoelectric legs and the substrate).

Due to parasitic conduction heat transfer between hot and cold junctions, and the thermal and electrical contact resistances, thin films (less than 1 μm) have not been used in conventional column-type thermoelectric coolers. These problems can be minimized, if thicker films (2–10 μm) are used. Here, the column-type design of a layered-fabricated micro-thermoelectric cooler is considered for a wireless vapor sensor application, as shown in Fig. 1. The thermoelectric films (Bi_2Te_3 and Sb_2Te_3) are about 4 μm thick (obtained from preliminary fabrication studies, by co-evaporation of the elements). The goal for the cooler is to lower the temperature of the sensor 10 K below ambient in less than 30 s, while using minimal power with a 3 V battery.

In this study, we consider how the small size of the columns will affect the thermal and electrical transport (electron, phonon and energy conversion) through the interfaces between the thermoelectric and metal films, and thus the performance of the device. Boundaries hinder the phonon heat flow differently than the electronic

* Corresponding author. Tel.: +1-734-936-0402; fax: +1-734-647-3170.

E-mail address: kaviany@umich.edu (M. Kaviany).

0017-9310/$ - see front matter © 2003 Elsevier Ltd. All rights reserved.
doi:10.1016/j.ijheatmasstransfer.2003.11.024

Nomenclature

a	unit cell dimension (m), side length (m)
A_k	cross-sectional area of the thermoelectric element (m^2)
$A_{j=1,4}$	constants in the electron and phonon temperature equations [Eqs. (19) and (20)]
B	emission constant (A/m^2 K^2)
c	unit cell dimension (m)
COP	coefficient of performance
d	side width (m), barrier thickness (m)
e_c	electronic charge 1.6022×10^{-19} C
E	electron energy (J)
E_c	energy at bottom of conduction band (J)
E_F	Fermi energy (J)
E_g	band gap energy (J)
E_o	potential barrier height (J)
E_v	energy at top of valence band (J)
f	frequency (Hz)
h_P	Planck constant 6.6261×10^{-34} J s
J_e	electrical current (A)
j_e	electrical current density (A/m^2)
k	thermal conductivity (W/m K)
k_B	Boltzmann constant 1.3806×10^{-23} J/K
L	thickness (m), Lorenz number (V^2/K^2)
$m_{e,o}$	electron mass in free space 9.1096×10^{-31} kg
$m_{e,te}$	electron/hole effective mass in the thermoelectric element (kg)
n	number density of primitive cells (m^{-3})
n_c	electron/hole concentration in the thermoelectric element (m^{-3})
N	donor/acceptor atom concentration (m^{-3})
N_{te}	number of thermoelectric pairs
P	density of states (s/rad m^3), tunneling probability
P_e	electrical power (W)
q	heat flux (W/m^2)
Q	heat flow rate (W)
R_e	electrical resistance (Ω)
R_k	conduction resistance (K/W)
$\dot{S}_e$	energy conversion rate (W)
T	temperature (K)
T_{ctc}	center-of-thermal-conductivity temperature (K)
u	velocity (m/s)
V_b	built-in potential energy (J)
W	depletion width (m)
Z_e	figure of merit (1/K)

Greek symbols

α_S	Seebeck coefficient (V/K)
γ	k_e/k_p
δ	electron–phonon cooling length (m)
$\Delta\varphi$	voltage (V)
ϵ_o	free-space permittivity 8.8542×10^{-12} C^2/J m
ϵ_r	relative permittivity
μ	electron/hole mobility (m^2/V s)
ρ_e	electrical resistivity (Ω m)
τ	transmission coefficient
τ_e	electron/hole energy relaxation time (s)
τ_m	electron/hole momentum relaxation time (s)
ϕ	work function (J)
χ	electron affinity (J)
ω	angular frequency (rad/s)

Subscripts

b	boundary
c	cold, contact
cc	cold connector
D	Debye
e	electron
h	hot
hc	hot connector
j	phonon mode
J	Joule
l	load
m	metal
mc	metal connector
n	n-type thermoelectric material
p	p-type thermoelectric material, phonon
P	Peltier
te	thermoelectric element
∞	ambient

Superscript

*	dimensionless

heat flow, causing the two subsystems to be out of thermal equilibrium [7]. As the thickness of the thermoelectric film decreases and becomes comparable to the carrier cooling length, this electron–phonon non-equilibrium becomes significant, and influences the thermoelectric properties of the device.

The phonon and electron boundary resistances and the phonon–electron non-equilibrium adjacent to the interfaces of the thermoelectric elements have been described by others [7–13]. Molecular dynamics, lattice dynamics, Boltzmann transport equation, and Monte Carlo methods, have all been used as tools to understand heat conduction mechanisms and to simulate the nanoscale transport process [14,15]. Here, the phonon boundary resistance is estimated by the diffuse mismatch model theory using the measured density of states [8,9].

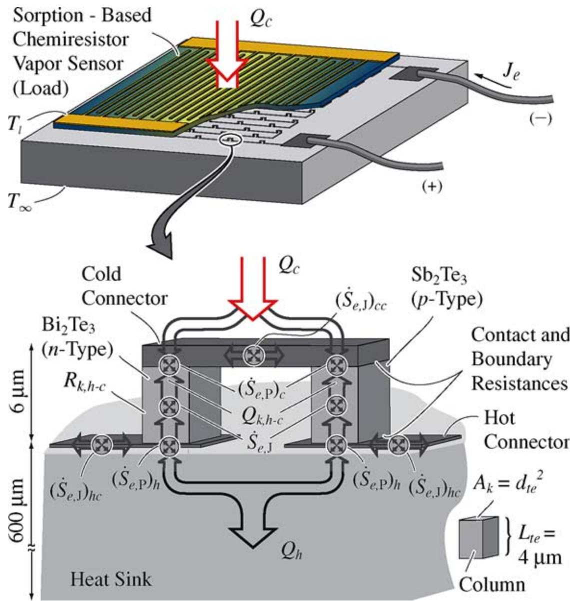

Fig. 1. Rendering of micro-thermoelectric cooler used with a micro-vapor sensor. The column-type design and various energy conversion mechanisms $\dot{S}_e$ and heat transfer Q are also shown.

The electron boundary resistance is estimated assuming electron tunneling and using the Wiedemann-Franz law at the boundaries [7]. The electron and phonon temperature distributions in the thermoelectric elements are obtained from a simplified form of the coupled Boltzmann transport equations for the electron and phonon subsystems [7,10,13]. In addition, the thermal and electrical contact resistances (due to defects in the crystal structure, variation of surface roughness, etc, originated in the fabrication process) are estimated from the experimental results reported in the literature [16–22].

Based on these interfacial effects, the flows of heat and electricity in the micro-cooler are modeled. An optimal geometry is obtained, and the overall device performance is predicted. These results will be used in the ongoing fabrication research (not reported here).

2. Thermal and electrical transport at boundaries

The interface of a conductor and a thermoelectric material is characterized by a mismatch in bulk properties and by irregularities in the thin region near the boundary. Different thermal and electrical carriers encounter different resistances across this interfacial region.

Phonons (quanta of energy associated with lattice vibrations) are assumed to strike the interface and lose their memory. The probability of being scattered to one side of the interface or the other is related to the density of states and the phonon speeds of different modes. The phonon boundary resistance represents the reflected phonons and is considered independent of the interface structure [8].

Electrons are assumed to encounter a potential barrier at the interface (which depends on the band structure of the two interfacial materials), resulting in the electron boundary resistance. For a metal/semiconductor interface absent of surface states, the potential barrier height is a function of the metal work function (energy required to excite an electron from the Fermi level to the vacuum level), the semiconductor electron affinity (energy difference between the highest energy level in the conduction band and the vacuum level) and the semiconductor bandgap (energy gap that separates the conduction band from the valence band) [23]. The potential barrier width (or thickness) depends on the metal work function, and on the semiconductor permittivity, doping density and work function. Depending on the height and thickness of the potential barrier, electrons can tunnel through this barrier or be thermally excited over it (thermionic emission) [7].

Phonon and electron boundary resistances at a metal/thermoelectric interface cause electron–phonon thermal non-equilibrium near the boundary, which is most significant in the thermoelectric material (the transport of heat in the metal is accomplished by the free conduction electrons). The energy conversion mechanisms (Joule heating and Peltier cooling/heating) will also contribute to this non-equilibrium [7]. In crystalline thermoelectric materials, electrons will interact with phonons and impurities, and in the polycrystalline state, with phonons, impurities and grain boundaries. These cause the electrons to reach thermal equilibrium with the lattice (phonons), at a distance from the interface known as the cooling length.

The phonon and electron boundary resistances (related to the thermal transport) are present only at the metal/thermoelectric interfaces, and their effects are included in the physical properties of the thermoelectric elements. Interfacial features not included in the boundary resistances (e.g., surface defects, crystal size and orientation, strain in the materials), depend on the fabrication process. These affect both the thermal and the electrical transport through the interfaces, and are included in the thermal and electrical contact resistances. These contact resistances are present at all interfaces and are directly added to the bulk resistance of the metal connectors.

3. Boundary resistances

Heat is transferred across a continuous solid junction by electrons and phonons. The thermal boundary resistances associated with thermoelectric heat transport

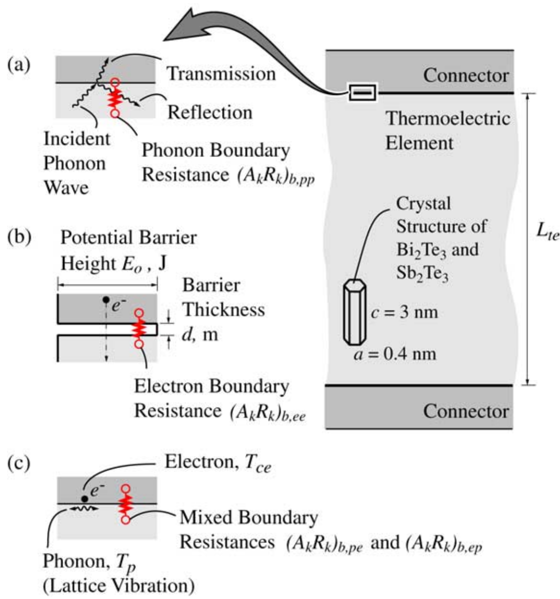

Fig. 2. Thermal boundary resistances associated with phonon and electron heat transport at the metal/thermoelectric interface: (a) phonon boundary resistance, (b) electron boundary resistance, (c) mixed boundary resistances.

through metal/semiconductor interfaces are presented in Fig. 2. A phonon wave incident at the interface will be partially transmitted (and partially reflected) due to the mismatch between the properties of the two materials. This phonon wave reflection causes the phonon boundary resistance $(A_kR_k)_{b,pp}$, as shown in Fig. 2(a), where A_k is the cross-sectional area of the thermoelectric element, R_k is the conduction resistance, and the subscript b,pp stands for the resistance at the boundary in the phonon subsystem. An electronic potential barrier of thickness d and height E_o, associated with the different band structures of the two materials, is shown in Fig. 2(b). This barrier represents a resistance to the electronic heat transport across the interface, i.e., the electron boundary resistance $(A_kR_k)_{b,ee}$. Energy can also be directly exchanged between phonons (on one side of the interface) and electrons (on the other side). The resistance associated with this energy transfer is the mixed boundary resistance $(A_kR_k)_{b,pe}$, or $(A_kR_k)_{b,ep}$, as shown in Fig. 2(c).

3.1. Phonon boundary resistance

In the current application, the interface is formed by a thermoelectric material (Bi_2Te_3 or Sb_2Te_3) and a conductor (metal connector), which have different density of states (DOS), mass density, Debye temperature and frequency, and also different speeds of sound, providing resistance to the flow of phonons at the interface.

Two theories have been applied to the prediction of the phonon boundary resistance [8]. The first is the acoustic mismatch model (AMM), which assumes no phonon scattering (i.e, a perfect, planar interface with specular reflection). The second one is the diffuse mismatch model (DMM), which assumes that all phonons incident on the interface will scatter (i.e., a rough interface with diffuse reflections). In the AMM, the transport is controlled by the difference in the acoustic impedance of the materials (product of the mass density and the phonon velocity). The assumption that no scattering occurs at the interface is reasonable at very low temperatures, where the phonon wavelength is longer than other interface length scales such as defects and roughness. As the temperature increases the phonon wavelength decreases, compromising the AMM theory. In the DMM, the transport is controlled by the diffuse scattering at the interface and the differences in densities of states.

Phelan [9] showed that by using the measured phonon DOS (as compared to the DOS calculated assuming the Debye model), the DMM predicts the phonon boundary resistance $R_{k,b,pp}$ in relatively good agreement with the experimental data. Here we will use the DMM and show that by using our estimated average phonon speed for the thermoelectric material, the measured DOS and that of the Debye model give similar values of $R_{k,b,pp}$.

The physical system consists of a film (material te, thermoelectric element) deposited on a substrate (material mc, metal connector). In a typical application, a net heat flux q is caused by the increase of the film temperature T_{te}, relative to the substrate temperature T_{mc}. The heat flux and temperatures are related through

$$(A_kR_k)_{b,pp} = \frac{T_{te} - T_{mc}}{q}. \tag{1}$$

Starting with the general expression for the energy transported per unit time from material te to material mc, and assuming that the transmission coefficient $\tau_{te\to mc}$ is independent of the temperature on either side of the interface (only one side of the interface is considered) [8], Phelan [9] derived an expression for q as a function of the phonon DOS P_p:

$$q = \frac{h_P \tau_{te\to mc}}{8\pi} \sum_j u_{p(te,j)} \int_0^\infty P_p(\omega_p)\omega_p \left[\frac{1}{\exp\left(\frac{h_P\omega_p}{2\pi k_B T_{te}}\right)} - \frac{1}{\exp\left(\frac{h_P\omega_p}{2\pi k_B T_{mc}}\right)} \right] d\omega_p. \tag{2}$$

In Eq. (2), h_P is the Planck constant, j is the phonon mode (either longitudinal or transverse), $u_{p(te,j)}$ is the speed of the phonon of mode j in material te, ω_p is the phonon angular frequency, and k_B is the Boltzmann

Table 1
Bulk properties of n- and p-type thermoelectric elements

Property	Reference	Bi_2Te_3	Sb_2Te_3
T_D, K	[25]	165	160
a, m	[25]	4.38×10^{-10}	4.25×10^{-10}
c, m	[25]	30.36×10^{-10}	29.96×10^{-10}
$\alpha_{S,bulk}$, μV/K	[2]	−228	171
k, W/m K	[7]	2.0	2.1
k_e, W/m K	[7]	0.5	0.6
k_p, W/m K	[7,16,17]	1.5	1.5
ρ_e, Ω m	[2]	1.30×10^{-5}	1.04×10^{-5}
μ, m^2/V s	[2]	75×10^{-4}	173×10^{-4}
$m_{e,te}$, kg	[16]	$0.58m_{e,o}$	$m_{e,o}$
n_c, m^{-3}	[2]	6.5×10^{25}	3.4×10^{25}

constant. The transmission coefficient is approximated by [8,9]

$$\tau_{te\to mc} = \frac{\sum_j u_{p(mc,j)}^{-2}}{\sum_j u_{p(te,j)}^{-2} + \sum_j u_{p(mc,j)}^{-2}}. \quad (3)$$

Note that Eq. (3) is derived for the case where T_{te} is equal to T_{mc} [9], whereas here there is a finite heat flow rate through the thermoelectric film. So, Eq. (3) would give an adequate prediction of the transmission coefficient for small $T_{te} - T_{mc}$. Our typical heat flow rates give $T_{te} - T_{mc}$ approximately equal to or less than 1 K. We use $T_{te} - T_{mc}$ equal to 1 K and Eq. (3) in the present study. However, as also reported by Phelan [9], no significant change in the phonon boundary resistance is found above 90 K, for $T_{te} - T_{mc}$ up to 10 K.

Equation (2) is numerically integrated to yield a value for q, which is substituted into Eq. (1) to determine $(A_kR_k)_{b,pp}$. Due to the lack of data for material te (here, either Sb_2Te_3 or Bi_2Te_3), and since the fabricated films are polycrystalline (verified by X-ray diffraction), we have assumed that the three phonon wave speeds (two transverse and one longitudinal) are equal, i.e.,

$$\sum_j u_{p(te,j)}^{-2} = \frac{1}{u_{p(te,l)}^2} + \frac{2}{u_{p(te,t)}^2} = \frac{3}{u_{p(te)}^2}. \quad (4)$$

The phonon speed u_p is related to the Debye temperature T_D, and to the Debye angular frequency ω_D, through the expressions

$$T_D = \frac{h_P\omega_D}{2\pi k_B} \quad \text{and} \quad \omega_D = (6\pi^2 u_p^3 n)^{1/3}, \quad (5)$$

where n is the ratio between the number of primitive cells and the unit cell volume.

For Bi_2Te_3 and Sb_2Te_3, the non-primitive hexagonal unit cell with dimensions a and c contains three lattice points and has three times the volume of the primitive rhombohedral cell [24]. The numerical values of the lattice parameters a and c, as well as the Debye temperature [25] used for determining the average phonon speed and the transmission coefficient of material te are given in Table 1. The material mc, assumed to be copper, has longitudinal and transverse phonon speeds equal to 4760 and 2,325 m/s respectively [26]. The results obtained from Eqs. (3) and (5) are presented in Table 2. Bulat [27] has assumed that for bismuth compounds the sound velocity is 2100 m/s, which is approximately 30% lower than the values predicted here.

The measured [28] and the Debye phonon DOS, P_p (THz^{-1}), as a function of the phonon frequency f_p (THz) for the thermoelectric materials Bi_2Te_3 and Sb_2Te_3 are shown in Fig. 3(a). To establish P_p as a function of the angular frequency ω_p and on a per unit volume basis [i.e., P_p given in (s/rad m^3)], as required by Eq. (2), the values shown in the graph are divided by 2π and multiplied by the factor n, defined after Eq. (5). The Debye DOS $P_{p,D}$ (s/rad m^3) is given by

$$P_{p,D} = \frac{\omega_p^2}{2\pi^2 u_p^3}. \quad (6)$$

From the areas under the curves of the Fig. 3(a), we have predicted the boundary resistances using the Debye ($f_p < f_{p,D} = 3.3$ THz) and the measured DOS (0.1 THz $\lesssim f_p \lesssim 5.2$ THz), and have found similar values, as shown in Fig. 3(b). The difference in the resistances reported by Phelan [9] may be due to the lack of agreement between the areas under the curves (for $YBa_2Cu_3O_{7-\delta}$ used there). In that analysis, ω_D is to the left of the measured mean frequency, i.e, $\omega_D = 5.4 \times 10^{13}$ rad/s

Table 2
Microscale properties of n- and p-type thermoelectric elements

Property	Bi_2Te_3	Sb_2Te_3
n, m^{-3}	5.95×10^{27}	6.40×10^{27}
ω_D, rad s^{-1}	2.16×10^{13}	2.09×10^{13}
u_p, m s^{-1}	3,058	2,888
$\tau_{te\to mc}$	0.56	0.54
τ_m, s	2.5×10^{-14}	9.8×10^{-14}
τ_e, s	1.0×10^{-11}	2.7×10^{-11}

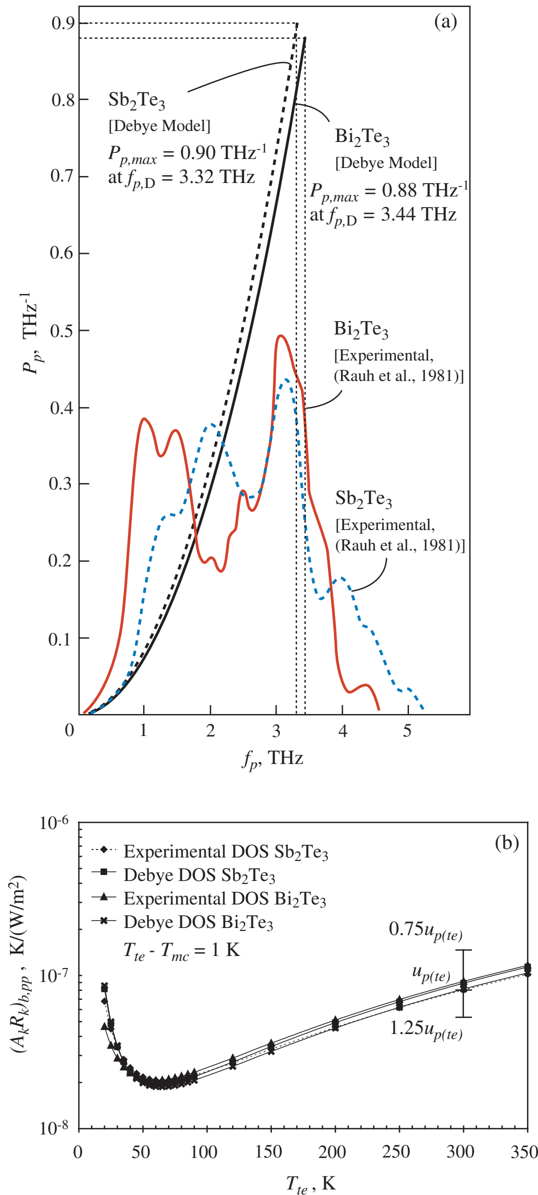

Fig. 3. (a) Variation of the phonon density of states P_p of n- and p-type thermoelectric elements with respect to phonon frequency f_p. (b) Variation of the phonon boundary resistance $(A_k R_k)_{b,pp}$ of n- and p-type thermoelectric elements with respect to the temperature T_{te}. The markers are to guide the eye.

and the measured DOS ranges from 1×10^{13} to 14×10^{13} rad/s. The increase in the boundary resistance with increase in temperature (at high temperatures) has also been reported by Prasher and Phelan [29]. They developed a new model that incorporates near boundary scattering (due to non-uniformities) in the basic acoustic mismatch model. The thermal boundary resistance at higher temperatures is successfully predicted using an empirical Umklapp scattering parameter. Since no experimental boundary resistance data is available for Bi_2Te_3 and Sb_2Te_3, this model is not used here. It should also be mentioned that the observed minimum in Fig. 3(b) moves to the right, as the Debye temperature increases, and then a plateau behavior is reached, as shown in [9].

In order to assess the effect of any uncertainty in $u_{p(te)}$ on $R_{k,b,pp}$, ±25% variation is allowed in $u_{p(te)}$ of Sb_2Te_3. In Fig. 3(b), it is shown that $R_{k,b,pp}$ decreases 33% and increases 82% (at $T_{te} = 300$ K) when $u_{p(te)}$ increases and decreases 25% respectively.

For T_{te} equal to 300 K, the phonon boundary resistances at the Bi_2Te_3/Cu and Sb_2Te_3/Cu interfaces, determined using the experimental DOS, are 9.2×10^{-8} K/(W/m^2) and 8.0×10^{-8} K/(W/m^2), respectively. These resistances have the same order of magnitude of the resistances measured by Stoner and Maris [30] (1.0×10^{-8}–3.2×10^{-8} K/(W/m^2) at 300 K) between diamond and several metals.

3.2. Electron boundary resistance

When a metal is in contact with a semiconductor, the Fermi energy levels in the two materials must be the same at thermal equilibrium. In addition, the vacuum level must be continuous. These two requirements determine a unique energy band diagram for the ideal metal–semiconductor contact [31]. The energy band diagrams of a metal with work function ϕ_m, and of n- and p-type semiconductors with work functions ϕ_n and ϕ_p, and electron affinities χ_n and χ_p, are shown in Fig. 4(a), for $\phi_p > \phi_m > \phi_n$. When the solids come into contact (Fig. 4(b)), the more energetic electrons in the conduction band (CB) of the n-type semiconductor will diffuse into the metal in search of lower empty energy levels (just above the metal Fermi energy $E_{F,m}$) and accumulate near the surface of the metal. Electrons flowing from the semiconductor leave behind an electron-depleted region of width W. In this region, the difference between the energy at the bottom of the conduction band and the Fermi energy of the n-type semiconductor $(E_{c,n} - E_{F,n})$ must increase, so that the concentration of electrons $n_{c,n}$ decreases $\{n_{c,n} \sim \exp[-(E_{c,n} - E_{F,n})/k_B T]\}$ [32]. The bands must bend to increase $E_{c,n} - E_{F,n}$ toward the junction. The potential barrier for electrons moving from the metal to the n-type semiconductor is $E_{o,n} = \phi_m - \chi_n$, and is greater than the built-in potential energy $V_{b,n}$ (energy needed to take an electron from the n-type semiconductor to the metal). Eventually this built-in potential reaches a value that prevents further accumulation of the electrons at the metal surface and an equilibrium is reached. Similarly, electrons in the metal will cross the junction to the p-type semiconductor searching for lower energy levels

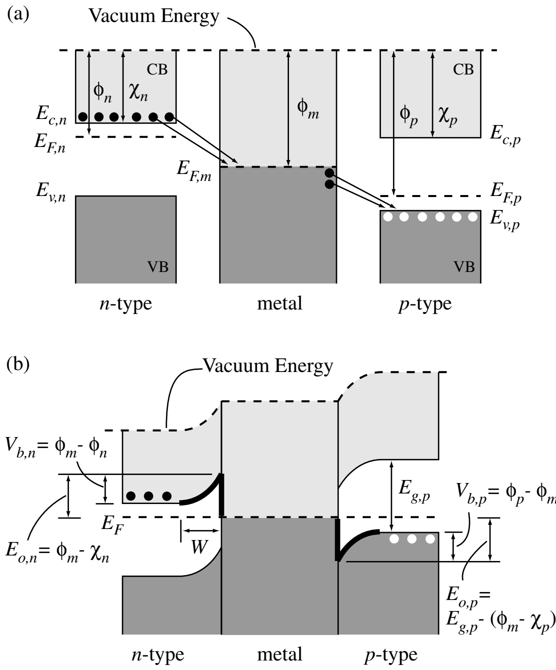

Fig. 4. Electron energy bands for a metal and *n*- and *p*-type semiconductors, (a) before, and (b) after contact. The potential barrier is marked with the heavy lines.

around $E_{v,p}$ (energy at the top of the valence band of the *p*-type semiconductor). To show the decrease of hole concentration $n_{c,p}$ near the junction, the *p*-type semiconductor energy bands are bent downward to increase $E_{F,p} - E_{v,p}\{n_{c,p} \sim \exp[-(E_{F,p} - E_{v,p})/k_B T]\}$ [32]. The potential barrier for electrons moving from the metal to the *p*-type semiconductor is $E_{o,n} = E_{g,p} - (\phi_m - \chi_p)$, where E_g is the band gap energy.

In the present study, the electron boundary resistance is modeled using a potential barrier with a rectangular shape [7], where we take E_o (which can be either $E_{o,n}$ or $E_{o,p}$) as the potential barrier height, and $W/2$ as the potential barrier thickness d. The electrons can be transferred across this barrier by tunneling. In analogy with the Wiedemann–Franz law, the electron boundary resistance is given by

$$\frac{1}{(A_k R_k)_{b,ee}} = \frac{\pi^2}{3} \frac{T}{(A_k R_e)_b} \left(\frac{k_B}{e_c}\right)^2, \tag{7}$$

where $(A_k R_e)_b$ is the electrical boundary resistance [7],

$$\frac{1}{(A_k R_e)_b} = \frac{4\pi e_c^2 m_{e,te} P}{h_P^3} \left[\frac{h_P^2 E_o}{8\pi^2 m_{e,te} d^2}\right]^{1/2}, \tag{8}$$

$m_{e,te}$ is the effective mass of the electrons/holes in the thermoelectric material (given in Table 1), e_c is the electronic charge, and P is the tunneling probability. Tunneling occurs if [7]

$$\left[\frac{h_P^2 E_o}{(8\pi^2 m_{e,te} d^2)}\right]^{-1/2} k_B T \ll 1. \tag{9}$$

For thick barriers the dominant transport mechanism is thermionic emission. Then, $\pi^2/3$ in Eq. (7) is replaced by 2, and the electrical boundary resistance is given by [7]

$$\frac{1}{(A_k R_e)_b} = \frac{e_c B T e^{-E_o/k_B T}}{k_B}, \tag{10}$$

where B is equal to 120×10^4 A/m^2 K^2, and E_o is assumed to be much larger than $k_B T$ [23].

In order to choose between tunneling and thermionic emission, E_o and d must be estimated. Mahan and Woods [33] have reported potential barriers between some metals and semiconductors equal to or less than 0.1 eV, including a Bi_2Te_3/Sb_2Te_3 interface (0.035 eV). Nagao et al. [34], have reported that ohmic contact characteristics are observed at the Au/Bi_2Te_3 junction, i.e, no Schottky barrier is formed, so the contact does not limit the current flow. These two results indicate that small barriers can be obtained with such semiconductors. Here, we assume E_o equal to 0.1 eV at the interfaces between the metal and both thermoelectric materials. Both Bi_2Te_3 and Sb_2Te_3 are narrow-gap semiconductors ($E_{g,n} = 0.15$ eV and $E_{g,p} = 0.2$ eV) [35,36], and the assumed value (0.1 eV) is lower than their energy gaps. This same relation was verified by the comparison with reported values of E_o for various other metal/semicondutor interfaces [23,37] and E_g of the respective semiconductors [23].

The barrier thickness d is estimated from the depletion width W ($d = W/2$), which can be approximated (for zero applied voltage) as [31]

$$W = \left(\frac{2\epsilon_r \epsilon_o E_o}{e_c N}\right)^{1/2}, \tag{11}$$

where ϵ_r is the relative permittivity of the semiconductor, which is equal to 100 for Bi_2Te_3 [38] and equal to 55 for Sb_2Te_3 [39], ϵ_o is the free-space permittivity (8.8542×10^{-12} C^2/J m) and N is the donor/acceptor atom concentration in the crystal. When N is much larger than the concentration of the intrinsic semiconductor (pure semiconductor crystal in which the electron and hole concentrations are equal), then N is nearly equal the carrier concentration n_c (electrons in the *n*-type semiconductor and holes in the *p*-type semiconductor) [32], which is given in Table 1. Assuming that this is the case here (i.e., $N \approx n_c$), d is found to be 2.06 nm (metal/Bi_2Te_3) and 2.12 nm (metal/Sb_2Te_3).

From Eq. (9), we verify that tunneling will occur if $d \ll 3.1$ nm and $d \ll 2.4$ nm for the *n*- and *p*-type semiconductor/metal junctions respectively. Although the values of d obtained from Eq. (11) are slightly smaller than these obtained from Eq. (9), we assume

tunneling as the electron transport mechanism here, and therefore, we use Eqs. (7) and (8) to evaluate the electron boundary resistance.

The tunneling probability is given by [31]

$$P = \left\{ 1 + \frac{E_o^2 \sinh^2 [8\pi^2 m_{e,te}(E_o - E)d^2/h_P^2]^{1/2}}{4E(E_o - E)} \right\}^{-1}, \qquad (12)$$

where E is the electron energy (measured from the bottom of the potential barrier), and $E < E_o$. Taking $E = E_o/2 = 0.05$ eV (i.e., $E \approx 2k_BT$), we obtain P values of 0.104 and 0.031 at the metal/Bi_2Te_3 and metal/Sb_2Te_3 junctions, respectively.

The resistances $(A_kR_e)_b$ and $(A_kR_k)_{b,ee}$ are then estimated from Eqs. (8) and (7) respectively, and are 2.6×10^{-12} $\Omega\,m^2$ and 3.5×10^{-7} K/(W/m^2) at the metal/Bi_2Te_3 interface, and 6.8×10^{-12} $\Omega\,m^2$ and 9.3×10^{-7} K/(W/m^2) at the metal/Sb_2Te_3 interface.

3.3. Total boundary resistance

The total thermal boundary resistance $(A_kR_k)_b$ is given by [7]

$$\frac{1}{(A_kR_k)_b} = \frac{1}{(A_kR_k)_{b,pp}} + \frac{1}{(A_kR_k)_{b,ee}} + \frac{1}{(A_kR_k)_{b,ep}} + \frac{1}{(A_kR_k)_{b,pe}}. \qquad (13)$$

Assuming for simplicity that there is no direct heat transfer between electron and phonon subsystems across the boundary, i.e., $R_{k,b,pe}$ and $R_{k,b,ep} \to \infty$, the total thermal boundary resistance will be a function of the phonon and electron boundary resistances only. In this case, at the Bi_2Te_3/Cu and Sb_2Te_3/Cu interfaces, the total thermal boundary resistances are 7.2×10^{-8} K/(W/m^2) and 7.4×10^{-8} K/(W/m^2), respectively.

4. Phonon–electron non-equilibrium

Because the thermal boundary resistances of the electrons and phonons are not the same, and due to ohmic heating and Peltier cooling/heating, electrons and phonons can have different temperatures adjacent to the interface ($T_e \neq T_p$) and require a distance δ (the cooling length) to equilibrate. This phonon–electron non-equilibrium region is shown in Fig. 5.

4.1. Cooling length

The cooling length δ, which is the distance from the boundary required for electrons and phonons to reach equilibrium, is defined as [10,27]

$$\delta = \left[\frac{\tau_e}{n_c k_B} \frac{k_e k_p}{(k_e + k_p)} \right]^{1/2}, \qquad (14)$$

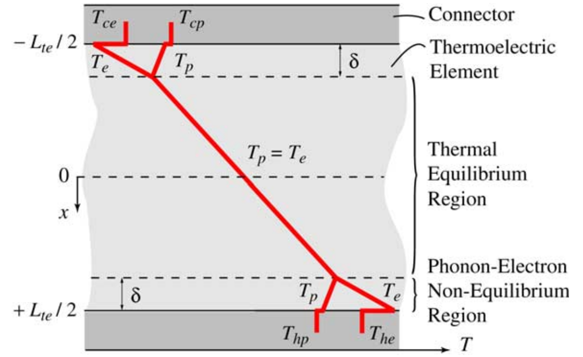

Fig. 5. Schematic phonon–electron non-equilibrium adjacent to the boundary due to the mismatch of the electron and phonon boundary resistances, Joule heating, and Peltier heating/cooling.

where τ_e is the electron/hole energy relaxation time, and k_e and k_p are the electron and phonon contributions to the thermal conductivity k ($k = k_e + k_p$). Bartkowiak and Mahan [7] have reported k_e and k_p equal to 0.5 W/m K and 1.5 W/m K, respectively, for Bi_2Te_3. For Sb_2Te_3, we assume the same phonon contribution (i.e, $k_p = 1.5$ W/m K) [16,17], and estimate the electronic contribution using the Wiedemann–Franz law, $k_e = LT/\rho_e$, where L is the Lorenz number and ρ_e is the electrical resistivity. For L equal to 2.1×10^{-8} V^2/K^2 at 300 K [40] and ρ_e equal to 1.04×10^{-5} $\Omega\,m$, we have k_e equal to 0.6 W/m K.

The electron/hole energy relaxation time is given by [27,41]

$$\tau_e = \frac{k_B T}{2m_{e,te}u_p^2}\tau_m, \qquad (15)$$

where u_p is the phonon speed estimated in Section 3.1, and τ_m is the electron/hole momentum relaxation time, which is a function of the electron/hole mobility μ [27,32],

$$\tau_m = \frac{m_{e,te}\mu}{e_c}. \qquad (16)$$

The properties of the n- and p-type thermoelectric elements used to evaluate the relaxation times and cooling length are given in Table 1. The results obtained from Eqs. (15) and (16) are presented in Table 2. The cooling lengths estimated for Bi_2Te_3 and Sb_2Te_3 are 66 and 156 nm, respectively.

The available values for mobility vary from 75×10^{-4} to 1200×10^{-4} m^2/V s for Bi_2Te_3, and from 173×10^{-4} to 510×10^{-4} m^2/V s for Sb_2Te_3 [2,16]. Note also, that the cooling length depends on u_p^2. Based on the values considered here for μ and u_p, the predicted cooling lengths are on the lower side, which is a conservative result, as will be shown in Section 5.

4.2. Phonon and electron temperatures

The kinetics of electrons and phonons in an electric field or in a temperature field is described by the coupled Boltzmann equations for electrons and phonons [10]. For a one-dimensional geometry, these equations can be given by

$$-k_e \frac{d^2 T_e}{dx^2} = \rho_e j_e^2 - \frac{n_c k_B}{\tau_e}(T_e - T_p), \tag{17}$$

$$-k_p \frac{d^2 T_p}{dx^2} = \frac{n_c k_B}{\tau_e}(T_e - T_p), \tag{18}$$

where j_e is the electrical current density. These are the equations of energy balance in the electron and phonon subsystems.

Assuming that ρ_e, n_c, τ_e, k_e and k_p are constant, the above equations are solved by defining a center-of-thermal-conductivity temperature $kT_{ctc} = k_e T_e + k_p T_p$, [7]. The solution is

$$T_e = A_1 + A_2 \frac{x}{L_{te}} + \frac{\rho_e j_e^2 \left[\left(\frac{L_{te}}{2}\right)^2 - x^2\right]}{2k} + \frac{\rho_e j_e^2 \delta^2}{\gamma k} - \frac{1}{\gamma}\left[A_3 \cosh\left(\frac{x}{\delta}\right) + A_4 \sinh\left(\frac{x}{\delta}\right)\right], \tag{19}$$

$$T_p = A_1 + A_2 \frac{x}{L_{te}} + \frac{\rho_e j_e^2 \left[\left(\frac{L_{te}}{2}\right)^2 - x^2\right]}{2k} - \frac{\rho_e j_e^2 \delta^2}{k} + \left[A_3 \cosh\left(\frac{x}{\delta}\right) + A_4 \sinh\left(\frac{x}{\delta}\right)\right], \tag{20}$$

where $\gamma = k_e/k_p$, and L_{te} is the thermoelectric element thickness.

The four unknown constants A_1, A_2, A_3 and A_4 are determined by the boundary conditions for the flow of heat by electrons and phonons at the boundaries, as presented in Fig. 6(a) and (b). Note that, as previously discussed, no direct heat transfer between electrons and phonons across the boundaries is considered, i.e, $R_{k,b,ep} = R_{k,b,pe} \to \infty$. Also for simplicity, it is assumed that electrons and phonons are in equilibrium in the connectors, i.e, $T_{cp} = T_{ce} = T_c$ and $T_{hp} = T_{he} = T_h$.

The phonon boundary conditions are, at $x = -L_{te}/2$,

$$-\frac{\left[T_c - T_p\left(-\frac{L_{te}}{2}\right)\right]}{(A_k R_k)_{b,pp}} - k_p \left.\frac{dT_p}{dx}\right|_{-\frac{L_{te}}{2}} = 0, \tag{21}$$

and at $x = L_{te}/2$,

$$-\frac{\left[T_p\left(\frac{L_{te}}{2}\right) - T_h\right]}{(A_k R_k)_{b,pp}} - k_p \left.\frac{dT_p}{dx}\right|_{\frac{L_{te}}{2}} = 0. \tag{22}$$

The electron boundary conditions are, at $x = -L_{te}/2$,

$$-\frac{\left[T_c - T_e\left(-\frac{L_{te}}{2}\right)\right]}{(A_k R_k)_{b,ee}} - k_e \left.\frac{dT_e}{dx}\right|_{-\frac{L_{te}}{2}} + (\alpha_{S,bulk} - \alpha_{S,b}) \times j_e T_e\left(-\frac{L_{te}}{2}\right) - (A_k R_e)_b \frac{j_e^2}{2} = 0, \tag{23}$$

and at $x = L_{te}/2$,

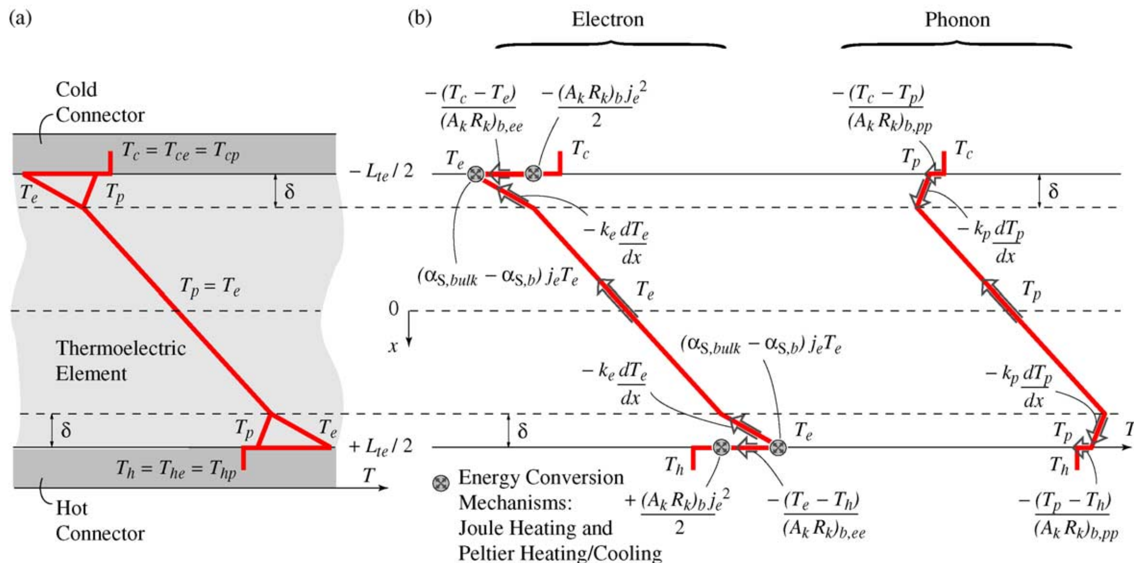

Fig. 6. (a) Schematic temperature distribution of electrons and phonons assuming equilibrium in the connectors. (b) Energy conversion mechanisms and heat transfer path of the electron and phonon subsystems.

$$-\frac{\left[T_e\left(\frac{L_{te}}{2}\right)-T_h\right]}{(A_kR_k)_{b,ee}}-k_e\frac{\mathrm{d}T_e}{\mathrm{d}x}\bigg|_{\frac{L_{te}}{2}}+(\alpha_{S,bulk}-\alpha_{S,b})\times j_eT_e\left(\frac{L_{te}}{2}\right)+(A_kR_e)_b\frac{j_e^2}{2}=0. \quad (24)$$

The first term in the above equations represents the heat flow as defined by the phonon (electron) boundary resistance, and the second term is the heat flow predicted by the Fourier law. The third term of Eqs. (23) and (24) represents the Peltier cooling and heating, respectively. The Joule heating at the boundaries is represented by the fourth term.

The bulk Seebeck coefficient $\alpha_{S,bulk}$ is given in Table 1 for the n- and p-type thermoelectric materials. The boundary Seebeck coefficient $\alpha_{S,b}$, assuming that tunneling is the dominant electron transport mechanism across the metal/semiconductor interfaces, is given by [7]

$$\alpha_{S,b}=\left(\frac{k_{\mathrm{B}}}{e_c}\right)\frac{\pi^2}{3}k_{\mathrm{B}}T\left[\frac{h_{\mathrm{P}}^2E_o}{8\pi^2m_{e,te}d^2}\right]^{-1/2}. \quad (25)$$

Taking the values of E_o and d estimated in Section 3.2, we find $|\alpha_{S,b}|$ equal to 252 and 187 μV/K for the p- and n-type semiconductor/metal junctions, respectively. (The sign of $\alpha_{S,b}$ is discussed in Section 5.2).

Eqs. (19) and (20) were solved analytically with Eqs. (21)–(24). The resulting expressions for the coefficients A_j are in general very complicated. For electrical current j_e equal to zero, the coefficients A_j are

$$A_1=\frac{T_h+T_c}{2}, \quad (26)$$

$$A_2=\frac{\gamma L_{te}^*\coth L_{te}^*+\frac{R_e^*R_p^*(1+\gamma)^2}{2R_k^*}}{R_e^*+\frac{R_e^*R_p^*(1+\gamma)^2}{2R_k^*}+\frac{\gamma L_{te}^*\coth L_{te}^*}{(1+2R_k^*)^{-1}}+R_p^*\gamma^2}\times(T_h-T_c), \quad (27)$$

$$A_3=0, \quad (28)$$

$$A_4=\frac{\gamma^2R_p^*-\gamma R_e^*}{R_e^*+\frac{R_e^*R_p^*(1+\gamma)^2}{2R_k^*}+\frac{\gamma L_{te}^*\coth L_{te}^*}{(1+2R_k^*)^{-1}}+R_p^*\gamma^2}\times\frac{(T_h-T_c)}{2\sinh L_{te}^*}, \quad (29)$$

where the dimensionless parameters (*) are given by

$$R_e^*=\frac{R_{k,b}}{R_{k,b,ee}},\quad R_p^*=\frac{R_{k,b}}{R_{k,b,pp}},\quad R_k^*=\frac{R_{k,b}}{\frac{L_{te}}{A_kk}},\quad L_{te}^*=\frac{L_{te}}{2\delta}. \quad (30)$$

The electron and phonon temperatures for j_e equal to 0, 15 and 30 mA are shown in Fig. 7. Note that at the cold junction ($x=-2$ μm), the electron temperature decreases with Peltier cooling and increases with Joule heating [Eq. (23)]. At the hot junction ($x=2$ μm), the electron temperature is increased by both of these energy conversions [Eq. (24)], which explains the larger deviations of T_e and T_p from the temperature in this junction (T_h), compared with the smaller deviations of T_e and T_p from the temperature in the cold junction (T_c). The difference between T_e and T_p increases as j_e increases, as expected by inspection of Eqs. (19) and (20). The distance from the junctions (hot or cold) required for electrons and phonons to reach equilibrium, i.e, where $T_e=T_p$, is larger (for j_e not equal to zero) than the cooling length of 156 nm estimated for Sb_2Te_3. This is due to the effects of Joule heating, not considered in the derivation of Eq. (14). This difference increases (i.e., δ becomes larger) with the increase of j_e.

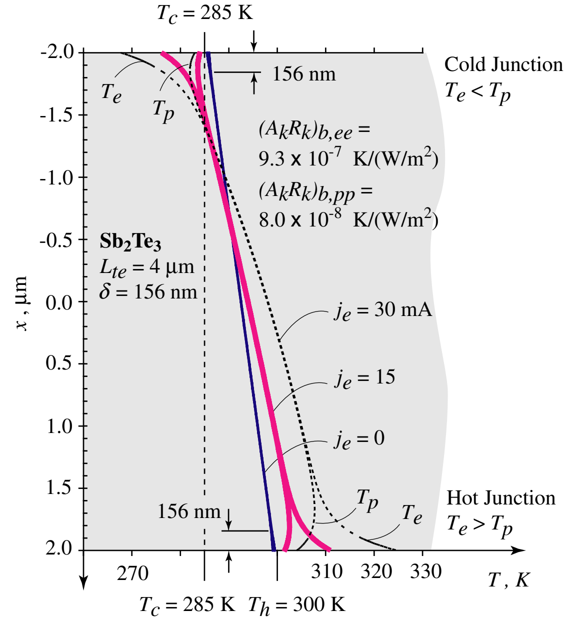

Fig. 7. Phonon and electron temperature distributions in the Sb_2Te_3 thermoelectric element [Eqs. (19) and (20)].

5. Effect of boundary resistances and phonon–electron non-equilibrium on thermoelectric properties

The efficiency of the n- and p-type thermoelectric elements is determined by the figure of merit

$$Z_e=\frac{\alpha_S^2}{\rho_ek}=\frac{\alpha_S^2}{R_{e,h\text{-}c}/R_{k,h\text{-}c}}, \quad (31)$$

where $R_{e,h\text{-}c}$ and $R_{k,h\text{-}c}$ are the electrical and thermal resistances, respectively. A low electrical resistance is desired in order to minimize the Joule heating, $\dot{S}_{e,\mathrm{J}}$, and the electrical power consumption, P_e, of the device. The thermal resistance must be large to minimize the undesirable conduction heat transfer from the hot junction to the cold junction, $Q_{k,h\text{-}c}$, shown in Fig. 1. The Seebeck

coefficient α_S is an indicator of the device thermopower, i.e., the Peltier heating/cooling at the junctions, $\dot{S}_{e,P}$, and should be maximized.

Here, as the thermoelectric element has a small thickness ($L_{te} = 4$ μm), its thermoelectric properties, and therefore, its efficiency, can be influenced by the boundary effects (phonon and electron boundary resistances and phonon–electron non-equilibrium).

5.1. Thermal resistance of thermoelectric element

In the absence of electrical current, the heat flow across the thermoelectric element i ($i = n, p$) can be calculated as

$$Q_{k,h\text{-}c}(j_e = 0) = \frac{(T_h - T_c)}{(R_{k,h\text{-}c})_i}. \quad (32)$$

From the heat flow path shown in Fig. 6(b),

$$Q_{k,h\text{-}c}(j_e = 0) = A_k\left[-k_e\frac{\mathrm{d}T_e}{\mathrm{d}x} - k_p\frac{\mathrm{d}T_p}{\mathrm{d}x}\right]_{-\frac{L_{te}}{2}} = A_k\left[-k_e\frac{\mathrm{d}T_e}{\mathrm{d}x} - k_p\frac{\mathrm{d}T_p}{\mathrm{d}x}\right]_{\frac{L_{te}}{2}}. \quad (33)$$

Therefore, the thermal resistance of the thermoelectric elements is given by

$$(R_{k,h\text{-}c})_i = \left[\frac{(T_h - T_c)}{A_k\left[-k_e\frac{\mathrm{d}T_e}{\mathrm{d}x} - k_p\frac{\mathrm{d}T_p}{\mathrm{d}x}\right]_{\frac{L_{te}}{2}}}\right]_i = \left[\frac{L_{te}}{A_k k}\frac{(T_h - T_c)}{A_2}\right]_i, \quad (34)$$

or, introducing Eq. (27) into Eq. (34),

$$\frac{(R_{k,h\text{-}c})_i}{\frac{L_{te}}{A_k k_i}} = \left[\frac{R_e^* + \frac{R_e^* R_p^*(1+\gamma)^2}{2R_k^*} + \frac{\gamma L_{te}^* \coth L_{te}^*}{(1+2R_k^*)^{-1}} + R_p^*\gamma^2}{\gamma L_{te}^* \coth L_{te}^* + \frac{R_e^* R_p^*(1+\gamma)^2}{2R_k^*}}\right]_i. \quad (35)$$

Note that $R_{k,h\text{-}c}$ is greater than the bulk resistance $L_{te}/(A_k k)$ due to the thermal boundary resistances and the phonon–electron non-equilibrium. This increase in $R_{k,h\text{-}c}$ reduces the undesirable heat conduction from the hot to the cold junctions. For L_{te} much greater than 2δ, Eq. (35) becomes

$$\frac{(R_{k,h\text{-}c})_i}{\frac{L_{te}}{A_k k_i}} = \left[1 + \frac{2R_{k,b}}{\frac{L_{te}}{A_k k}}\right]_i. \quad (36)$$

The effect of the cooling length and the phonon and electron boundary resistances on the thermal resistance $R_{k,h\text{-}c}$, which is obtained from Eqs. (35) and (36), is shown in Fig. 8(a), for cases (i)–(iv) described below. The increase in $R_{k,h\text{-}c}$, compared to the bulk resistance, is only 7.2% for (i) the predicted resistances [$(A_k R_k)_{b,pp} = 9.2 \times 10^{-8}$ K/(W/m^2) and $(A_k R_k)_{b,ee} = 3.5\times 10^{-7}$ K/(W/m^2)] and cooling length ($\delta = 66$ nm) of the Bi_2Te_3 thermoelectric element. An increase of these resistances by an order of magnitude (iv), increases $R_{k,h\text{-}c}$ in 72%. Note that δ can significantly affect $R_{k,h\text{-}c}$ only when $R_{k,b,pp}$ (iii) or $R_{k,b,ee}$ (ii) are individually increased, and $\delta \gtrsim 100$ nm. The thermal resistance of the thermoelectric element is more sensitive to the increase of $R_{k,b,pp}$ (iii). In this case, $R_{k,b,pp}$ is greater than $R_{k,b,ee}$, and the total thermal boundary resistance [Eq. (13)] is dominated by the electron contribution. The shaded region in the graph marks the range in which the cooling length is varied as a function of the phonon speed of Bi_2Te_3 ($u_{p,te}$ estimated in Section 3.1 is equal to 3058 m/s).

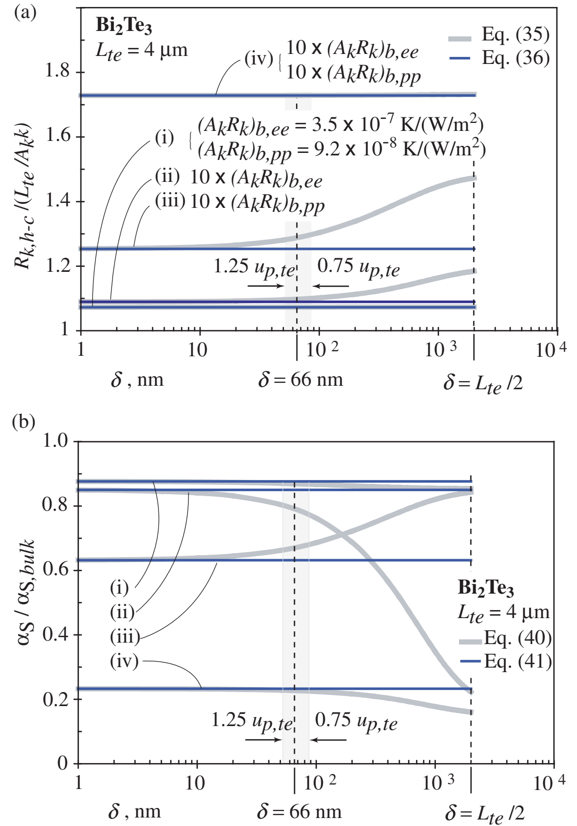

Fig. 8. Variation of (a) thermal resistance, $R_{k,h\text{-}c}$, obtained from Eqs. (35) and (36), and (b) Seebeck coefficient of the thermoelectric element, α_S, obtained from Eqs. (40) and (41), with respect to the cooling length δ, and electron $(A_k R_k)_{b,ee}$ and phonon $(A_k R_k)_{b,pp}$ boundary resistances.

5.2. Seebeck coefficient of thermoelectric element

The Seebeck coefficient of the thermoelectric element i ($i = n, p$) is given by

$$\alpha_{S,i} = \frac{\Delta\varphi_{h\text{-}c}}{T_h - T_c}, \quad (37)$$

where $\Delta\varphi_{h-c}$ is the voltage drop between the cold and hot interfaces of the element due to the bulk and boundaries Seebeck effects, i.e.,

$$\Delta\varphi_{h-c} = \alpha_{S,b}[T_h - T_e(L_{te}/2)] + \alpha_{S,bulk}[T_e(L_{te}/2) - T_e(-L_{te}/2)] + \alpha_{S,b}[T_e(-L_{te}/2) - T_c]. \quad (38)$$

Therefore, Eq. (37) becomes

$$\alpha_{S,i} = \left[\alpha_{S,b} + \frac{\left[T_e\left(\frac{L_{te}}{2}\right) - T_e\left(-\frac{L_{te}}{2}\right)\right]}{T_h - T_c}(\alpha_{S,bulk} - \alpha_{S,b})\right]_i, \quad (39)$$

or, after evaluating T_e at the cold and hot interfaces [Eq. (19)],

$$\alpha_{S,i} = \left[\alpha_{S,b} + \frac{R_e^* + \frac{R_e^* R_p^*(1+\gamma)^2}{2R_k^*} + \gamma L_{te}^* \coth L_{te}^* - R_p^*\gamma}{R_e^* + \frac{R_e^* R_p^*(1+\gamma)^2}{2R_k^*} + \frac{\gamma L_{te}^* \coth L_{te}^*}{(1+2R_k^*)^{-1}} + R_p^*\gamma^2} \times (\alpha_{S,bulk} - \alpha_{S,b})\right]_i. \quad (40)$$

For $\delta \ll L_{te}/2$,

$$\alpha_{S,i} = \left[\alpha_{S,b} + \frac{1}{\frac{2k(A_k R_k)_b}{L_{te}} + 1}(\alpha_{S,bulk} - \alpha_{S,b})\right]_i. \quad (41)$$

Note that for j_e equal to zero, $[T_e(L_{te}/2) - T_e(-L_{te}/2)]$ is less than or equal to $(T_h - T_c)$, as shown in Fig. 7. Therefore, it is implied from Eq. (39) that $|\alpha_{S,i}| \leqslant |\alpha_{S,bulk}|$. This defines the sign of the boundary Seebeck coefficients obtained from Eq. (25), i.e., $\alpha_{S,b}$ is equal to −252 and 187 μV/K for the *p*- and *n*-type semiconductor/metal junctions, respectively.

The effect of the cooling length and the boundary resistances on the Seebeck coefficient, which is obtained from Eqs. (40) and (41), is shown in Fig. 8(b), for the same four cases discussed in Section 5.1 [also indicated in Fig. 8(a)]. The effective Seebeck coefficient is lower than the bulk Seebeck coefficient, indicating an undesirable reduction on the thermoelectric energy conversion of the device. For the predicted boundary resistances (i) $[(A_k R_k)_{b,pp} = 9.2 \times 10^{-8}$ K/(W/m^2) and $(A_k R_k)_{b,ee} = 3.5 \times 10^{-7}$ K/(W/m^2)] and cooling length ($\delta = 66$ nm) of the Bi_2Te_3 thermoelectric element, a reduction of 13% is found in α_S. This proportion is increased to 77% when both electron and phonon boundary resistances are increased by an order of magnitude (iv). For $\delta < 10$ nm, the Seebeck coefficient is more sensitive to the increase in $R_{k,b,pp}$ (α_S is reduced by 37%, (iii)), than to the increase in $R_{k,b,ee}$ (α_S is reduced by 15%, (ii)), as observed for the thermal resistance of the thermoelectric element. However, for larger cooling lengths, the increase in the individual resistances cause opposite effects. While α_S is drastically decreased in case (ii), it is increased in case (iii), where the electron contribution to the total boundary resistance is dominant.

From Fig. 8(a) and (b), it is observed that for $R_{k,b,ee} < R_{k,b,pp}$ (iii), a larger cooling length [recall that δ was estimated on the conservative (lower) side] would result in higher thermoelectric efficiency [Eq. (31)], due to the increase in both the conduction resistance and the Seebeck coefficient of the thermoelectric elements. For δ equal to 66 nm, any increase in the boundary resistances results in opposite effects on $R_{k,h-c}$ and α_S, i.e., the conduction resistance is increased and the Seebeck coefficient is decreased. In Section 7, where the results from the device optimization are discussed, the device cooling performance will be investigated as a function of these combined effects. A decrease in the performance with an increase in the boundary resistances is expected, since the efficiency of the thermoelectric element is more sensitive to the reduction of α_S, than to the increase of $R_{k,h-c}$ [Eq. (31)].

6. Contact resistances

The thermal $(A_k R_k)_c$ and electrical $(A_k R_e)_c$ contact resistances are a result of impurities, variations in the crystal size and orientation, defects, etc, at the interface, which are created in the fabrication process. When a semiconductor is grown on top of a metal (or vice versa) there is often no gap at the interface. But the different lattice parameters of the materials allow strain between the layers, which may cause the dislocation of atoms and the formation of defects. Variation in the stoichiometry of the thermoelectric compounds, as well as diffusion of the metal into the semiconductor, can also occur. These surface features (not considered in the thermal boundary resistances) affect the transport of heat and electricity through the interfaces. Their effects must be included in the model for prediction of the micro-cooler performance, and here this is done through the introduction of $(A_k R_k)_c$ and $(A_k R_e)_c$. Both resistances cause a reduction of the device performance. Thermal and electrical contact resistances are present at the metal/thermoelectric interfaces, and thermal contact resistances are present at the metal/electrical–insulator interfaces of the micro-cooler. The effect of the thermal contact resistance is a discontinuity of temperature at the interface in the presence of a heat flow. An electrical contact resistance increases the total electrical resistance of the device, and generates Joule heating at the junctions. In practice, annealing (heat treatment) is used to reduce both the thermal and electrical contact resistances.

6.1. Thermal contact resistance

Lahmar et al. [18] performed an experimental investigation on the thermal contact resistance between a

gold coating and ceramic substrates, and showed that thermal treatment significantly increases the adhesion and reduces the thermal contact resistance between these materials. The contact resistance decreased from 10^{-7} K/(W/m^2) to less than 10^{-8} K/(W/m^2) after heat treatment.

Orain et al. [19] have developed a measurement technique for determining the thermal conductivity of dielectric thin films. It was reported that for films thicker than 1 μm, the film thermal conductivity is equivalent to the value for the bulk material. For thinner films, a drop in the conductivity was observed, revealing the importance of the film/substrate contact (and boundary) resistances. The effect of the layering technique and the nature of the metal and substrate on the contact resistance was also presented. Contacts of Au/Al_2O_3 and Au/SiO_2 formed by evaporation had resistances estimated on the order of 1 to 2×10^{-7} K/(W/m^2). Based on these results [18,19] a thermal contact resistance $(A_kR_k)_c$ of 10^{-7} K/(W/m^2) is assumed.

Note that, when interfacial thermal resistances are measured, the contributions of the contact and boundary resistances are difficult to distinguish. Therefore, the experimental results are for the dominant resistance, which we assume to be the contact resistance. If this is not the case, the predicted device performance will be lower than the expected (i.e, we have chosen the conservative side), as will be discussed in Section 7.

6.2. Electrical contact resistance

In macroscopic thermoelectric devices, electrical contact resistance between the semiconductor and metal electrodes has been reported to typically be between 10^{-8} and 10^{-9} $\Omega\,m^2$, when standard techniques for making a junction (such as soldering or hot pressing) are used [16,20]. However, films with micron or submicron thickness are produced using thin-film growth techniques (e.g., evaporation or sputtering), and the resistances are expected to be much smaller. Jaeger [21] has reported electrical contact resistances for a variety of aluminum-silicon systems, which range from 10^{-5} to 10^{-10} $\Omega\,m^2$ as a function of annealing temperature.

If it is assumed that there is no gap at the contact zone, then the electrical contact resistance $(A_kR_e)_c$ is that between the two materials at the interface [for example, Bi(Sb)–Te/metal]. Choosing the highest electrical resistivity between these materials, which is 1.3×10^{-5} $\Omega\,m$ (for Bi_2Te_3, as presented in Table 1), and estimating the length of the contact equal to 100 nm, results in $(A_kR_e)_c$ equal to 1.3×10^{-12} $\Omega\,m^2$.

The relation between the thermal (electronic contribution) and electrical resistances: $(A_kR_k)_{b,ee}$ and $(A_kR_e)_b$ when used for boundary resistances, or $(A_kR_k)_{c,e}$ and $(A_kR_e)_c$ when used for contact resistances, is given by Eq. (7). As indicated in Section 4.1, for Bi_2Te_3, the electron thermal conductivity k_e is 25% of the bulk thermal conductivity k [7]. Assuming the same contribution for the thermal contact resistances, we have $(A_kR_k)_{c,e} = 0.25\,(A_kR_k)_c$. Then, from Eq. (7), for $T = 300$ K, $(A_kR_e)_c$ is equal to 1.8×10^{-13} $\Omega\,m^2$.

Under well-controlled laboratory conditions, measured electrical contact resistance between Si and Pt has been reported to be 5×10^{-12} $\Omega\,m^2$, and between Si and Al, 1 to 2×10^{-11} $\Omega\,m^2$ [22]. Si/metal is not a type of electrical contact found in the thermoelectric cooler, but this is considered a good indication that the electrical resistivity of the Bi(Sb)–Te/metal contact can be less than or equal than 2×10^{-11} $\Omega\,m^2$, since the electrical resistivity of Si (10^{-4} $\Omega\,m$) is higher than that of the thermoelectric elements. Based on these results, $(A_kR_e)_c$ equal to 2×10^{-11} $\Omega\,m^2$ is assumed.

7. Geometry optimization

The heat flow path in the micro-thermoelectric cooler is shown in Fig. 1 and the various parameters used in the model are indicated in Fig. 9. Surface convection and radiation heat transfer between the heat sink and the vapor sensor are neglected as the conduction resistances of the films are much smaller than the surface radiation resistance and the air convection resistance (all in parallel). It is also assumed that the Joule heating in the thermoelectric material is equally split between the top and bottom bounding surfaces. So, at the cold junction we have [42]

$$Q_c + Q_{k,c\text{-}h} = (\dot{S}_{e,J})_c + (\dot{S}_{e,J})_{cc} + (\dot{S}_{e,P})_c, \quad (42)$$

and at the hot junction,

$$Q_h + Q_{k,h\text{-}c} = (\dot{S}_{e,J})_h + (\dot{S}_{e,J})_{hc} + (\dot{S}_{e,P})_h. \quad (43)$$

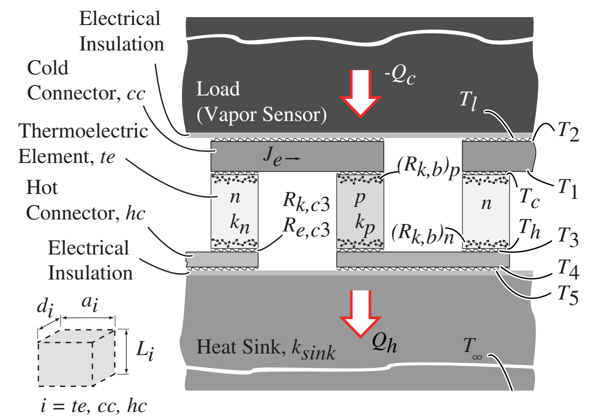

Fig. 9. Various parameters of the micro-thermoelectric cooler. The total boundary resistance $R_{k,b}$ (described in Section 3.3) at the thermoelectric/metal interfaces, and the contact resistances $R_{k,c}$ and $R_{e,c}$ (described in Section 6) at the thermoelectric/metal and metal/electrical–insulator interfaces are indicated.

$Q_{k,h\text{-}c}$ is the heat transferred from the hot to the cold surface by conduction,

$$Q_{k,h\text{-}c} = \frac{T_h - T_c}{R_{k,h\text{-}c}} = -Q_{k,c\text{-}h}. \quad (44)$$

The thermal resistance $R_{k,h\text{-}c}$ is given by

$$\frac{1}{R_{k,h\text{-}c}} = N_{te}\left[\frac{1}{(R_{k,h\text{-}c})_p} + \frac{1}{(R_{k,h\text{-}c})_n}\right], \quad (45)$$

where N_{te} is the number of thermoelectric pairs, and $(R_{k,h\text{-}c})_n$ and $(R_{k,h\text{-}c})_p$ are given by Eq. (35) as a function of the boundary resistances and cooling lengths estimated in Sections 3 and 4, respectively.

Q_c and Q_h are the heat transferred from the load (vapor sensor) to the cold surface and from the hot surface to the heat sink respectively:

$$Q_c = -\frac{T_l - T_c}{R_{k,c\text{-}l}} \quad \text{and} \quad Q_h = \frac{T_h - T_\infty}{R_{k,h\text{-}\infty}}. \quad (46)$$

At the cold side,

$$\frac{1}{R_{k,c\text{-}l}} = N_{te}\frac{1}{R_{k,c1} + R_{k,cc} + R_{k,c2}}, \quad (47)$$

and at the hot side,

$$\frac{1}{R_{k,h\text{-}\infty}} = N_{te}\frac{1}{R_{k,c3} + R_{k,hc} + R_{k,c4} + R_{k,sink}}. \quad (48)$$

Note that the thermal contact resistances between the thermoelectric elements and connectors are $(R_{k,c1})^{-1} = (R_{k,c3})^{-1} = 2A_k(k/L)_{contact}$ and between the connectors and the electrical insulator films are $(R_{k,c2})^{-1} = A_{cc}(k/L)_{contact}$ and $(R_{k,c4})^{-1} = A_{hc}(k/L)_{contact}$, where $(k/L)_{contact}$ was assumed equal to 10^7 (W/m^2)/K, as discussed in Section 6.1. The thermal resistances of the connectors are $(R_{k,i})^{-1} = (Ak/L)_i$, where $i = cc, hc$, and the thermal resistance of the heat sink (including the electrical insulator film), which was assumed an infinite solid, is $(R_{k,sink})^{-1} = \ln(4a_{hc}/d_{hc})/(\pi k_{sink} a_{hc})$ [42].

$(\dot{S}_{e,\text{P}})_c$ is the Peltier cooling at the cold junction and $(\dot{S}_{e,\text{P}})_h$ is the Peltier heating at the hot junction, given by

$$(\dot{S}_{e,\text{P}})_c = -N_{te}\alpha_S J_e T_c \quad \text{and} \quad (\dot{S}_{e,\text{P}})_h = N_{te}\alpha_S J_e T_h, \quad (49)$$

where J_e is the electric current flowing along the thermoelectric elements and metal connectors, and $\alpha_S = \alpha_{S,p} - \alpha_{S,n}$ is the sum of the Seebeck coefficients of the n- and p-type materials, which are given by Eq. (40).

$(\dot{S}_{e,\text{J}})_c$ and $(\dot{S}_{e,\text{J}})_h$ are the portions of the Joule heating (generated in the thermoelectric elements) assigned to the cold and hot junctions respectively. Note that the Joule heating generated at the metal/thermoelectric contacts is also considered, so that

$$(\dot{S}_{e,\text{J}})_c = (\dot{S}_{e,\text{J}})_h = \frac{1}{2}J_e^2 R_{e,h\text{-}c} + \frac{1}{2}J_e^2 R_{e,c}. \quad (50)$$

The electrical resistance of the thermoelectric elements is

$$R_{e,h\text{-}c} = N_{te}\left(\frac{\rho_{e,p}L_{te}}{A_k} + \frac{\rho_{e,n}L_{te}}{A_k}\right). \quad (51)$$

The contact electrical resistance is

$$R_{e,c} = \frac{4N_{te}(A_k R_e)_c}{A_k}, \quad (52)$$

where $(A_k R_e)_c$ is taken to be equal to 2×10^{-11} $\Omega\,\text{m}^2$, as discussed in Section 6.2.

$(\dot{S}_{e,\text{J}})_{cc}$ and $(\dot{S}_{e,\text{J}})_{hc}$ are the Joule heating generated in the cold and hot connectors respectively, given by

$$(\dot{S}_{e,\text{J}})_i = J_e^2 R_{e,i}, \quad \text{where } i = cc, hc, \quad (53)$$

$$R_{e,cc} = N_{te}\left(\frac{\rho_e a}{\text{d}L}\right)_{cc} \quad \text{and}$$
$$R_{e,hc} = N_{te}\left(\frac{\rho_e a}{\text{d}L}\right)_{hc} + R_{e,pads}. \quad (54)$$

Note that $R_{e,pads}$ is the electrical resistance between the contact pads and the initial thermoelectric structures of the cooler device. Based on measurements of preliminary fabricated structures, we have estimated $R_{e,pads}$ to be 50 Ω. Therefore, the total electrical resistance of the device can be expressed as

$$R_e = R_{e,h\text{-}c} + R_{e,cc} + R_{e,hc} + R_{e,c}, \quad (55)$$

and the total power consumed as

$$P_e = R_e J_e^2 + (\dot{S}_{e,\text{P}})_h + (\dot{S}_{e,\text{P}})_c = \Delta\varphi J_e, \quad (56)$$

where $\Delta\varphi$ is the total voltage required.

The coefficient of performance is given by

$$\text{COP} = -\frac{Q_c}{P_e}. \quad (57)$$

The calculations were performed with the thermal and electrical properties of the thermoelectric materials given in Table 1.

In Fig. 10, the current and voltage required as a function of the number of thermoelectric pairs are shown, for $T_l - T_\infty = 10$ K, $Q_c = -10$ mW, $L_{te} = 4$ μm, and $d_{te} = 7$, 9 and 11 μm ($A_k = d_{te}^2$). For $\Delta\varphi = 3$ V, the micro-cooler will need 30 to 60 thermoelectric pairs, as indicated by the shaded area. For $d_{te} = 7$ μm, the device operating current is lower than 20 mA. Note that the values of $T_l - T_\infty$ (10 K), Q_c (−10 mW) and $\Delta\varphi$ (3 V) are requirements of a specific application (cooling of a micro-chemiresistor vapor sensor), as indicated in Fig. 1. The height of the columns L_{te} (4 μm) is a result of preliminary fabrication studies. The minimum dimension of d_{te} (7 μm) has been chosen due to the limitations on the minimum feature size (3 μm) obtained in our microfabrication process.

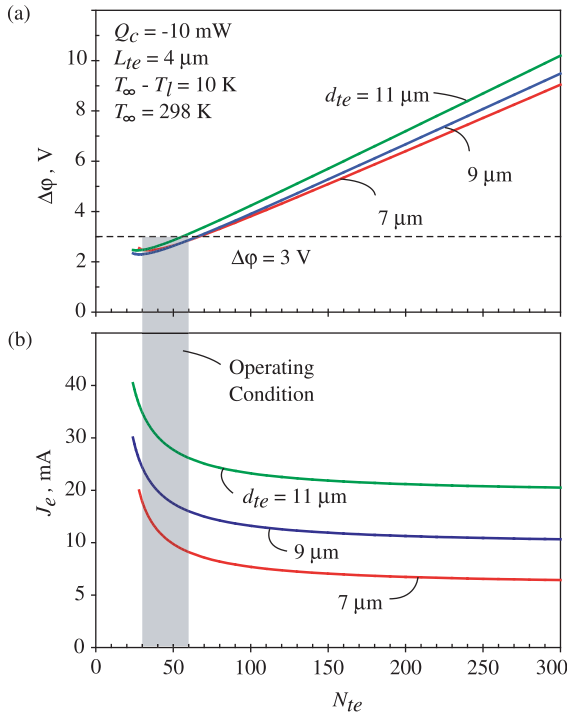

Fig. 10. Variation of required (a) voltage $\Delta\varphi$, and (b) current J_e, with respect to number of thermoelectric pairs N_{te}. The shaded region indicates the range of operating conditions for $\Delta\varphi$ equal to or smaller than 3 V.

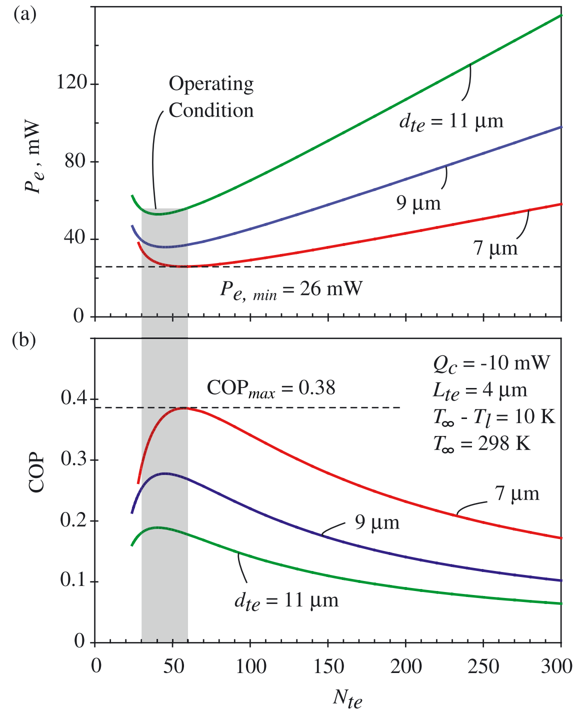

Fig. 11. Variation of (a) power requirement P_e, and (b) coefficient of performance COP, with respect to number of thermoelectric pairs N_{te}. The shaded region indicates the range of operating conditions for $\Delta\varphi$ equal to or smaller than 3 V.

The device power requirement and coefficient of performance, as a function of the number of thermoelectric pairs, are shown in Fig. 11. For $d_{te} = 7$ μm, the minimum power consumed $P_{e,min}$ is equal to 26 mW, which corresponds to a maximum coefficient of performance COP_{max} of 0.38. Typical COP values of commercially available thermoelectric modules are between 0.4 and 0.7 (for $L_{te} > 1$ mm). For devices with shorter thermoelectric elements, the performance is expected to be lower [43], as predicted here. The decrease in the device performance is due to the increase of both conduction heat transfer (from the hot to the cold junction) and resistance to the flow of electrons (which causes the undesirable Joule heating) with the increase of N_{te}. The selection of the cross-sectional area of the thermoelectric elements (i.e., d_{te}^2) is a compromise between reducing the conduction (a small area is desirable) and reducing the Joule heating (a large area is desirable).

For a given load Q_c, as the number of pairs increases, the current needed to achieve the desirable $(T_\infty - T_l)$ is decreased, since each thermoelectric pair receives a smaller portion of the load. This has a positive effect on the reduction of the power required [Eq. (56)], which when combined with the negative effect of the electrical resistance, results in the minimum power and the maximum coefficient of performance observed in Fig. 11.

Having defined the number of pairs as a function of the voltage [($N_{te} = 50$ pairs is chosen from Fig. 10(a)], and the side width of the columns for optimum performance ($d_{te} = 7$ μm is chosen from Fig. 11), the effect of the phonon boundary resistance $(A_k R_k)_{b,pp}$ and the electron boundary resistance $(A_k R_k)_{b,ee}$ on the reduction of the vapor sensor temperature is investigated. The results are shown in Fig. 12(a). The device cooling performance $(T_\infty - T_l)$ decreases with the increase of $(A_k R_k)_{b,ee}$, due to the reduction of the Seebeck coefficient, as presented in Fig. 8(b) [case (ii)], indicating that this effect is more pronounced on the performance than the increase of the thermal resistance shown in Fig. 8(a). As $(A_k R_k)_{b,ee}$ decreases, $(T_\infty - T_l)$ becomes less sensitive to the increase of $(A_k R_k)_{b,pp}$. The effects of the electron thermal transport [which dominates when $(A_k R_k)_{b,pp} \gg (A_k R_k)_{b,ee}$] on the boundary and bulk Seebeck coefficients, need to be further investigated.

Note that the variation in $(A_k R_k)_{b,ee}$ from 10^{-7} to 10^{-5} K/(W/m^2) in Fig. 12(a), corresponds to a variation in the potential barrier height E_o from approximately $0.5E_o$ to $1.5E_o$. The shaded area indicates the uncertainty in $(A_k R_k)_{b,pp}$ as a function of the phonon speed $u_{p,te}$. The dashed line indicates the operating condition, based on the values of the electron and phonon boundary

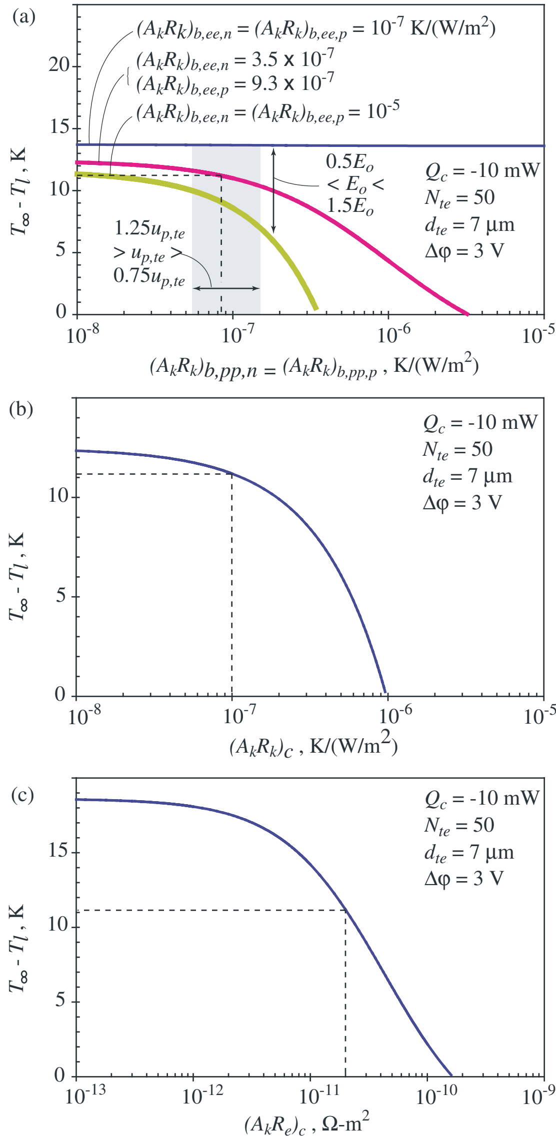

Fig. 12. Variation of the load temperature drop, $T_\infty - T_l$, with respect to (a) phonon boundary resistance $(A_kR_k)_{b,pp}$, (b) thermal contact resistance $(A_kR_k)_c$, and (c) electrical contact resistance $(A_kR_e)_c$. The shaded region indicates the uncertainty in $(A_kR_k)_{b,pp}$ as a function of the phonon speed of the thermoelectric element $u_{p,te}$. The dashed lines indicate the operating condition, based on the values of electron and phonon boundary resistances estimated in Section 3, and thermal and electrical contact resistances estimated in Section 6.

resistances estimated in Section 3. From the region defined by the shaded area and the curves, a minimum value for the device cooling performance $(T_\infty - T_l)$ of 7 K can be predicted.

In Fig. 12(b), the effect of the thermal contact resistance $(A_kR_k)_c$ on $(T_\infty - T_l)$ is presented. The value of $(A_kR_k)_c$ equal to 10^{-7} K/(W/m^2), which was estimated in Section 6.1, is indicated by the dashed line. An increase in $(A_kR_k)_c$ by one order of magnitude would reduce the cooling performance to zero. Note that this result is comparable with the effect of the thermal boundary resistances shown in Fig. 12(a), for the two cases with higher electron boundary resistance. In the Fig. 12(c), it is shown that increasing the electrical contact resistance $(A_kR_e)_c$ by one order of magnitude [$(A_kR_e)_c = 2 \times 10^{-11}$ Ω m^2 was estimated in Section 6.2, and is indicated by the dashed line] would also reduce the cooling performance $(T_\infty - T_l)$ to zero. Both thermal and electrical contact resistances can be diminished by improving the fabrication process and by post-fabrication treatments.

In Fig. 13, the effect of the film thickness L_{te} on the device cooling performance is presented. The optimum values observed are due to the opposite effects of increasing the electrical (undesirable) and conduction (desirable) resistances of the thermoelectric elements. The model predictions are based on $L_{te} = 4$ μm (indicated by the dashed line), which has been, so far, a fabrication limit. For $d_{te} = 7$ μm, which results in higher COP and lower power (as shown in Fig. 11), the maximum cooling performance can be reached when $L_{te} = 10$ μm. Based on this result, we will work towards increasing the thermoelectric film thickness.

In Fig. 14, the temperature distribution in the various films (Sb_2Te_3 is the thermoelectric material) that form the thermoelectric cooler is shown for $J_e = 11$ mA, which is obtained for $\Delta\varphi = 3$ V, $Q_c = -10$ mW and $N_{te} = 50$ pairs. The thicknesses of the films are not to scale. The temperature drop observed at the cold and hot interfaces (load/connector and connector/thermoelectric element) is a result of the thermal contact resistance $(A_kR_k)_c$ (estimated in Section 6.1). On the cold side (amplified region I), $(T_l - T_c) = 0.25$ K, and on the hot side (amplified region II), $(T_h - T_\infty) = 1.22$ K. In the

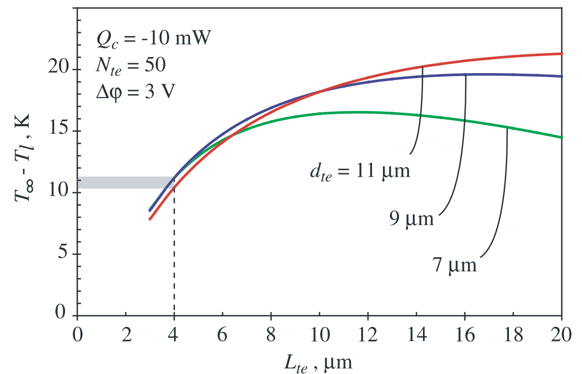

Fig. 13. Variation of the load temperature drop, $T_\infty - T_l$, with respect to thermoelectric element length L_{te}. The dashed line indicates the value of L_{te} (4 μm) used in the model for prediction of the micro-thermoelectric cooler operating condition.

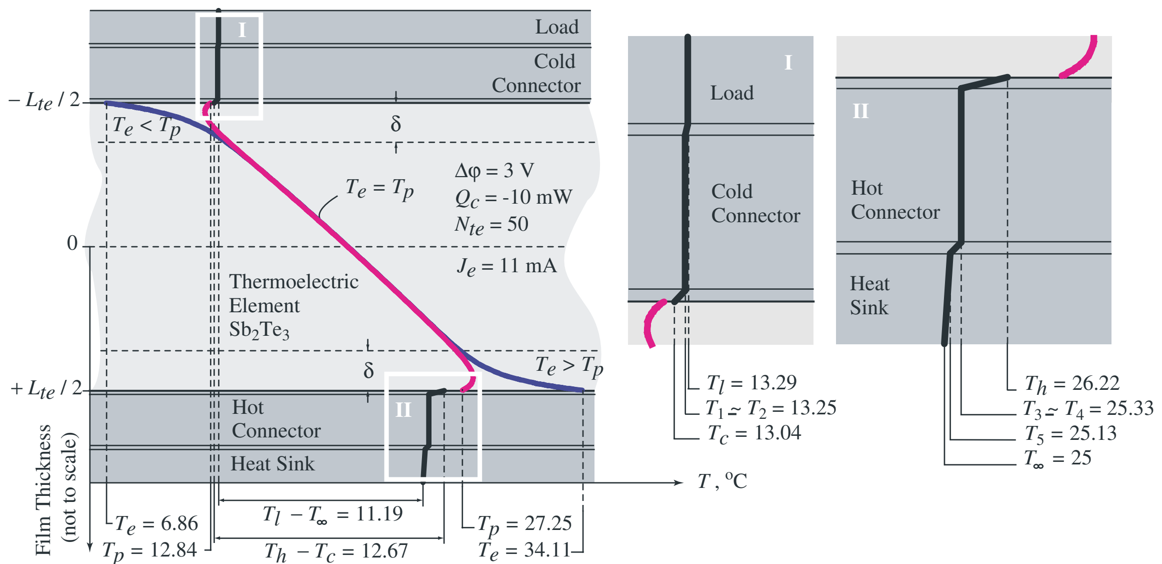

Fig. 14. Temperature distribution in the thermoelectric cooler. The film thickness (vertical axis) is not to scale.

thermoelectric element, the distributions of phonon temperature T_p and electron temperature T_e are shown, and the phonon–electron non-equilibrium near the boundaries is evident. This non-equilibrium depends on the phonon and electron boundary resistances, Peltier cooling/heating and Joule heating, as discussed in Section 4.2. At the cold junction $(T_p - T_e)$ is 5.98 K, and at the hot junction $(T_e - T_p)$ is 6.86 K. These large temperature differences indicate the importance of the thermal and electrical transport at the metal/thermoelectric interfaces when thin thermoelectric films are considered (here, $L_{te} = 4$ μm). The length of the non-equilibrium region is about 500 nm, which is much greater than $\delta = 156$ nm obtained from Eq. (14). This indicates that a more accurate estimation of the cooling length is needed.

8. Summary

In order to predict the performance of micro-thermoelectric coolers, various aspects of the electron and phonon transport have been addressed in this study.

The phonon boundary resistances estimated by the DMM theory, using the measured and Debye density of states, are similar, and have the same order of magnitude as the experimental values reported in the literature (for interfaces between diamond and several metals). For Bi_2Te_3/Cu and Sb_2Te_3/Cu interfaces, the phonon boundary resistances are found to be 9.2×10^{-8} and 8.0×10^{-8} K/(W/m^2), respectively. The electron boundary resistance is estimated as a function of the thickness and height of the electronic potential barrier, which is associated with the difference in the band structures of the two materials at the junction. Assuming electron tunneling and using the Wiedemann–Franz law at the boundaries, the electron boundary resistance is found to be 3.5×10^{-7} and 9.3×10^{-7} K/(W/m^2) at the *n*- and *p*-type semiconducor/metal interfaces, respectively. The cooling lengths of 66 nm (Bi_2Te_3) and 156 nm (Sb_2Te_3) are estimated using the available electron/hole mobility, phonon speed, and electron/hole concentration. The thermal and electrical contact resistances, estimated using the available experimental results in the literature, are 10^{-7} K/(W/m^2) and 2×10^{-11} Ω m^2, respectively.

The electron and phonon temperature distributions are obtained as a function of the predicted cooling lengths (δ), electron and phonon boundary resistances, Peltier heating/cooling, and Joule heating. The distance from the junctions (hot or cold) over which electrons and phonons reach equilibrium are found to be larger than δ. This is due to the Joule heating, not considered in the derivation of Eq. (14), and indicates that a more accurate model for predicting the cooling length is required. Also, from the temperature distribution shown in Fig. 14, a difference between the phonon and electron temperatures as high as 6.8 K is observed (and could be larger with an increase in current). The phonon–electron non-equilibrium at the metal/thermoelectric interface is evident, and indicates the importance of the thermal transport in the electron subsystem.

Since the predicted values of δ are more than one order of magnitude smaller than the thermoelectric

element thickness, the electron–phonon non-equilibrium does not significantly influence the thermal resistance and the Seebeck coefficient of the thermoelectric elements, as shown in Fig. 8. Although the phonon and electron boundary resistances reduce the conduction heat transfer along the columns, they also reduce the Peltier heating/cooling through the reduction of the Seebeck coefficient. The combined effect is the reduction of the device cooling capacity when the electron boundary resistance is larger than 10^{-7} K/(W/m^2) (which includes the values estimated in Section 3.2), as shown in Fig. 12(a). As the electron boundary resistance decreases, the thermal transport becomes dominated by the electron subsystem at the interface, causing the increase of the cooling performance. Based on these results, we believe that a further investigation of the electron boundary resistance and boundary Seebeck coefficient is needed. In addition, the direct heat transfer between electron and phonon subsystems across the boundary (which was assumed negligible, for simplicity, in Section 3.3), should be further investigated.

Although the discontinuities of temperature at the interfaces caused by the thermal contact resistances are small (compared to the electron–phonon non-equilibrium), as shown in Fig. 14 in the enlarged regions I and II, this resistance is an important factor affecting the device performance, as verified in Fig. 12(b). The electrical contact resistance is equally important. Both contact resistances are affected by the fabrication process (as discussed in Section 6), which can generate a greater uncertainty than that related to the prediction of the electron and phonon boundary resistances. Thus, we consider the thermal and electrical contact resistances the most critical parameters affecting the device performance.

The length of the thermoelectric element L_{te} (4 μm) has so far been limited by the film deposition method used. From Fig. 13, it is found that the aspect ratio L_{te}/d_{te} of the columns should be around 1.5 in order for the microcooler to provide optimal cooling. As d_{te} is constrained by the fabrication process to be equal to or larger than 7 μm, the film thickness should then be increased.

From the device optimization, it is predicted (for $\Delta\varphi$ equal to 3 V) that a micro-thermoelectric cooler with number of pairs N_{te} of 50, L_{te} of 4 μm, and d_{te} of 7 μm, should deliver a load Q_c of 10 mW with temperature of 11 K below the ambient. This device will require a power P_e of 34 mW, an electrical current J_e of 11 mA, and will have a coefficient of performance COP of 0.3.

Acknowledgements

This work was supported by the Engineering Research Center Program of the National Science Foundation under Award Number EEC-9986866, at the University of Michigan's Wireless Integrated Micro-Systems (WIMS) Center and by the Conselho Nacional de Desenvolvimento Cientifico e Tecnológico—CNPq, Brazil (L.W. da S.).

References

[1] H. Zou, D.M. Rowe, G. Min, Growth of *p*- and *n*-type bismuth telluride thin films by co-evaporation, J. Cryst. Growth 222 (2001) 82–87.

[2] H. Zou, D.M. Rowe, S.G.K. Williams, Peltier effect in a co-evaporated Sb_2Te_3(p)–Bi_2Te_3(n) thin film thermocouple, Thin Solid Films 408 (2002) 270–274.

[3] G. Min, D.M. Rowe, Cooling performance of integrated thermoelectric microcooler, Solid-State Electron. 43 (1999) 923–929.

[4] J.P. Fleurial, A. Borshchevsky, M.A. Ryan, W. Phillips, E. Kolawa, T. Kacisch, R. Ewell, Thermoelectric microcoolers for thermal management applications, Proceedings of the 16th International Conference on Thermoelectrics, 1997, pp. 641–645.

[5] J.P. Fleurial, J.A. Herman, G.J. Snyder, M.A. Ryan, A. Borshchevsky, C. Huang, Electrochemical deposition of $(Bi,Sb)_2Te_3$ for thermoelectric microdevices, Mater. Res. Soc. 626 (2000) Z11.3.1–Z11.3.8.

[6] D.-Y. Yao, C.-J. Kim, G. Chen, Spot cooling using thermoelectric microcoolers, Proceedings of the 18th International Conference on Thermoelectrics, 1999, pp. 256–259.

[7] M. Bartkowiak, G.D. Mahan, Heat and electricity transport through interfaces, in: Recent Trends in Thermoelectric Materials, vol. II, Semiconductors and Semimetals, vol. 70, Academic Press, New York, 2001, pp. 245–271.

[8] E.T. Swartz, R.O. Pohl, Thermal boundary resistance, Rev. Mod. Phys. 61 (3) (1989) 605–658.

[9] P.E. Phelan, Application of diffuse mismatch theory to the prediction of thermal boundary resistance in thin-film high-T_c superconductors, ASME J. Heat Transfer 120 (1998) 37–43.

[10] Y.G. Gurevich, O.L. Mashkevich, The electron–phonon drag and transport phenomena in semiconductors, Phys. Rep. (Rev. Sect. Phys. Lett.) 181 (6) (1989) 327–394.

[11] Y.G. Gurevich, G.N. Logvinov, Thermo-emf thermoelectric current in unipolar semiconductors with finite dimensions, Sov. Phys. Semicond. 26 (11) (1992) 1091–1094.

[12] V.S. Zakordonets, G.N. Logvinov, Thermoelectric figure of merit of monopolar semiconductors with finite dimensions, Semiconductors 31 (3) (1997) 265–267.

[13] L.P. Bulat, Thermoelectricity under large temperature gradients, J. Thermoelect. 4 (1997) 3–34.

[14] G. Chen, R. Yang, Nano-to-macroscale transport modeling through approximations, Proceedings of the 2002 ASME International Mechanical Engineering Congress and Exposition, IMECE2002-32120, 2002.

[15] D.G. Cahill, W.K. Ford, K.E. Goodson, G.D. Mahan, A. Majumdar, H.J. Maris, R. Merlin, S.R. Phillpot, Nanoscale thermal transport, J. Appl. Phys. 93 (2) (2003) 793–818.

[16] H.J. Goldsmid, Electronic Refrigeration, Pion, London, 1986.

[17] H.J. Goldsmid, Private communications, (2003).
[18] A. Lahmar, T.P. Nguyen, D. Sakami, S. Orain, Y. Scudeller, F. Danes, Experimental investigation on the thermal contact resistance between gold coating and ceramic substrates, Thin Solid Films 389 (2001) 167–172.
[19] S. Orain, Y. Scudeller, S. Garcia, T. Brousse, Use of genetic algorithms for the simultaneous estimation of thin films thermal conductivity and contact resistances, Int. J. Heat Mass Transfer 44 (2001) 3973–3984.
[20] D. Ilzycer, A. Sher, M. Shiloh, Electrical contacts to thermoelectric bismuth telluride based alloys, Proceedings of the 3rd International Conference on Thermoelectric Energy Conversion, 1980, pp. 200–202.
[21] R.C. Jaeger, Introduction to Microelectronic Fabrication, vol. V, Addison-Wesley, 1988.
[22] S. Wolf, Silicon Processing for the VLSI Era, Lattice Press, California, 1990.
[23] S.M. Sze, Physics of Semiconductor Devices, John Wiley & Sons, 1969.
[24] B.D. Cullity, Elements of X-ray Diffraction, second ed., Addison Wesley, 1978.
[25] D.M. Rowe, CRC Handbook of Thermoelectrics, CRC Press, 1995.
[26] D.R. Lide, CRC Handbook of Chemistry and Physics, 78th ed., CRC Press, 1997–1998.
[27] L. Bulat, Private communications (Literature in Russian), (2002).
[28] H. Rauh, R. Geick, H. Köhler, N. Nücker, N. Lehner, Generalized phonon density of states of the layer compounds Bi_2Se_3, Bi_2Te_3, Sb_2Te_3 and $Bi_2(Te_{0.5}Se_{0.5})_3$, $(Bi_{0.5}Sb_{0.5})_2Te_3$, Solid State Phys. 14 (1981) 2705–2712.
[29] R.S. Prasher, P.E. Phelan, A scattering-mediated acoustic mismatch model for the prediction of thermal boundary resistance, ASME J. Heat Transfer 123 (2001) 105–112.
[30] R.J. Stoner, H.J. Maris, Measurements of Kapitza conductance between diamond and several metals, Phys. Rev. Lett. 68 (10) (1992) 1563–1566.
[31] S.M. Sze, Semiconductor Devices—Physics and Technology, John Wiley & Sons, 1985.
[32] S.O. Kasap, Principles of Electronic Materials and Devices, second ed., McGraw Hill, 2002.
[33] G.D. Mahan, L.M. Woods, Multilayer thermionic refrigeration, Phys. Rev. Lett. 80 (18) (1998) 4016–4019.
[34] J. Nagao, E. Hatta, K. Mukasa, Evaluation of metal-Bi_2Te_3 contacts by electron tunneling spectroscopy, Proceedings of the 15th International Conference on Thermoelectrics, 1996, pp. 404–407.
[35] S.K. Mishra, S. Satpathy, O. Jepsen, Electronic structure and thermoelectric properties of bismuth telluride and bismuth selenide, J. Phys.: Condensed Matter 9 (1997) 461–470.
[36] V. Damodara Das, N. Soundararajan, Thermoelectric power and electrical resistivity of crystalline antimony telluride (Sb_2Te_3) thin films: temperature and size effects, J. Appl. Phys. 65 (6) (1989) 2332–2341.
[37] R.K. Willardson, A.C. Beer, in: Semiconductors and Semimetals, vol. 15 (Contacts, Junctions, Emitters), Academic Press, 1981.
[38] V. Sandomirsky, A.V. Butenko, R. Levin, Y. Schlesinger, Electric-field-effect thermoelectrics, J. Appl. Phys. 90 (5) (2001) 2370–2379.
[39] P. Lost'ak, C. Drasar, A. Krejcova, L. Benes, J.S. Dyck, W. Chen, C. Uher, Preparation and some physical properties of tetradymite-type Sb_2Te_3 single crystals doped with CdS, J. Cryst. Growth 222 (2001) 565–573.
[40] J.S. Dyck, W. Chen, C. Uher, Heat transport in $Sb_{2-x}V_xTe_3$ single crystals, Phys. Rev. B 66 (2002) 125206.
[41] M. Lundstrom, Fundamentals of Carrier Transport, second ed., Cambridge, 2000.
[42] M. Kaviany, Principles of Heat Transfer, Wiley, New York, 2001.
[43] G. Min, D.M. Rowe, Improved model for calculating the coefficient of performance of a Peltier module, Energy Convers. Manage. 41 (2000) 163–171.